Vortex coupling in trailing vortex-wing interactions

C. Chen, Z. Wang, and I. Gursul
Department of Mechanical Engineering, University of Bath, Bath BA2 7AY, United Kingdom

(Received 6 November 2017; published 28 March 2018)

The interaction of trailing vortices of an upstream wing with rigid and flexible downstream wings has been investigated experimentally in a wind tunnel, using particle image velocimetry, hot-wire, force, and deformation measurements. Counter-rotating upstream vortices exhibit increased meandering when they are close to the tip of the downstream wing. The upstream vortex forms a pair with the vortex shed from the downstream wing and then exhibits large displacements around the wing tip. This coupled motion of the pair has been found to cause large lift fluctuations on the downstream wing. The meandering of the vortex pair occurs at the natural meandering frequency of the isolated vortex, with a low Strouhal number, and is not affected by the frequency of the large-amplitude wing oscillations if the downstream wing is flexible. The displacement of the leading vortex is larger than that of the trailing vortex; however, it causes highly correlated variations of the core radius, core vorticity, and circulation of the trailing vortex with the coupled meandering motion. In contrast, co-rotating vortices do not exhibit any increased meandering.

DOI: 10.1103/PhysRevFluids.3.034704

I. INTRODUCTION

Interaction of streamwise vortices with downstream surfaces and wings commonly occurs in aeronautical and biological flows. Formation flight of birds [1,2] and fixed-wing aircraft [3,4] are well-known examples of such interactions. Other examples include fin-buffeting due to the leading-edge vortices [5], flight refueling, and interaction of canard-wing vortex with the main wing [6], which all belong to the general class of streamwise vortex-body interactions reviewed by Rockwell [7]. For these interactions, the sign of the upstream vortex and the sign of the tip vortex shed from the downstream wing (in the absence of an upstream vortex) may be the same (co-rotating vortices) or the opposite (counter-rotating vortices).

Recent computational simulations [8–10] and experiments [11] have led to better understanding of complex unsteady interactions of streamwise vortices with downstream wings. Depending on the relative location of the incident vortex with respect to the downstream wing, the vortex may form a dipole with the wing-tip vortex, split into two, or disintegrate due to the direct impingement. In some cases, a first helical mode instability developed in the incident vortex just upstream of the wing [8]. When the incident vortex is near the tip of the downstream wing, the vortex trajectory appears to be sensitive. Small changes in the location of the upstream wing can lead to significant variations in the trajectory [12,13]. The inherent unsteadiness of the incident vortex due to the displacements of the core, known as meandering or wandering, may dominate the vortex-wing interaction [12]. Long wavelength mode of the meandering may persist during the interaction and couple with the trailing vortex.

However, in previous investigations, displacements of the core of the incident vortices during the interaction appeared to be small, and time-averaged vortices seemed nearly axisymmetric, except in direct impingement. Here, in this paper, we report large-scale displacements of the incident vortex as it interacts with the downstream wing. This seemed to be due to the coupling of the incident vortex and the tip vortex shed from the downstream wing. The focus of this paper is the unsteady aspects of the vortex-vortex interactions.

A second objective is to investigate the possibility of vortex-wing coupling in the case of a flexible downstream wing. Upstream feedback of oscillating downstream surfaces on vortex breakdown of leading-edge vortices over delta wings is well known [14,15]. This is due to the subcritical nature of vortex flow downstream of breakdown, in which disturbances can propagate upstream [15,16]. Oscillations of flexible wings may provide feedback on the displacements of the incident vortex core and this remains as a realistic possibility. We have designed a flexible wing and investigated the interaction of trailing vortices with the flexible wing, with focus on the unsteady aspects.

Interactions of co-rotating and counter-rotating incident vortices with rigid and flexible downstream wings have been investigated in wind tunnel experiments. Particle image velocimetry (PIV), hot-wire, force, and deformation measurements have been carried out. We show early on in the paper that vortex unsteadiness is amplified only for counter-rotating incident vortices. Then we examine in detail the unsteady nature of the interaction with rigid and flexible wings.

II. EXPERIMENTAL APPARATUS AND METHODS

A. Experimental setup

The experiments were performed in an open test section wind tunnel located at the University of Bath. The wind tunnel has an outlet nozzle diameter of 0.76 m with a maximum speed of 20 m/s and a turbulence intensity of around 0.1% of the freestream velocity. The leading wing has a chord length of 100 mm and a span of 500 mm, resulting in a semiaspect ratio of $sAR = 5$. The trailing wing has a chord length $c = 100$ mm and a span of 400 mm, resulting in a semiaspect ratio of $sAR = 4$. Both the leading wing and the trailing wing have a cross-section profile of NACA 0012, and a flat wing tip. The rigid wing was made from 3D printed plastic and reinforced by two 8-mm steel rods. The flexible trailing wing was made from silicone gel and carbon fiber sandwich structure. Two halves were moulded separately and then glued together with a tailored carbon fiber reinforced plastic plate in the middle. The carbon fiber plate was designed to increase torsional stiffness to provide deformation predominantly in the bending mode. Several densities of silicone gel and layups of carbon fiber combinations were tested to achieve a natural frequency of the bending mode close to the meandering frequency of the incident vortex.

Both wings were mounted vertically (see Fig. 1). The leading wing was attached to an automatic traverse that features two translation rails for the y and z axis adjustments. The location of the trailing wing was fixed on a force balance against a large splitter plate (Fig. 1). The normal separation of the wings Δz is defined based on the distance between 30% chord line (pivot location) of the wings. The full range of the traverse allows a spanwise separation distance Δy range of -100 mm to 100 mm and a Δz range of -100 to 120 mm. The wing angle of attack can be adjusted from -15 deg to 15 deg. In the current experiments, the angle of attack of the upstream wing was varied as $\alpha_{LW} = \pm 5^\circ$ and $\pm 10^\circ$, while the angle of attack of the trailing wing was varied as $\alpha_{TW} = 5^\circ$ and 10°. The experiments were conducted at a constant streamwise separation, Δx, of 600 mm. All measurements were conducted at a freestream velocity of $U_\infty = 18.5$ m/s, and a Reynolds number based on the chord length Re $= 130{,}000$.

B. Particle image velocimetry (PIV) measurements

Particle Image Velocimetry measurements were carried out with a TSI 2D-PIV system. The system comprised a dual Nd:Yag 200 mJ laser and a 16 bit greyscale 3 312 × 2 488 pixel CCD digital camera. Seeding was provided with atomized olive oil particles. The camera was mounted inside the wind tunnel downstream of the test section on a rigid column. The mounting column was hard fixed to the laboratory floor and free from contact with the wind tunnel walls to eliminate vibration. In the PIV setup, the camera was fixed and calibrated for each laser sheet location. The camera was housed in a streamlined protective box to avoid oil damage and to minimize flow induced vibration. The laser was mounted on a traverse so that it could be moved along the streamwise direction for measurements in various crossflow planes ($x/c = -1.05$ to 0.05). The PIV system was operated

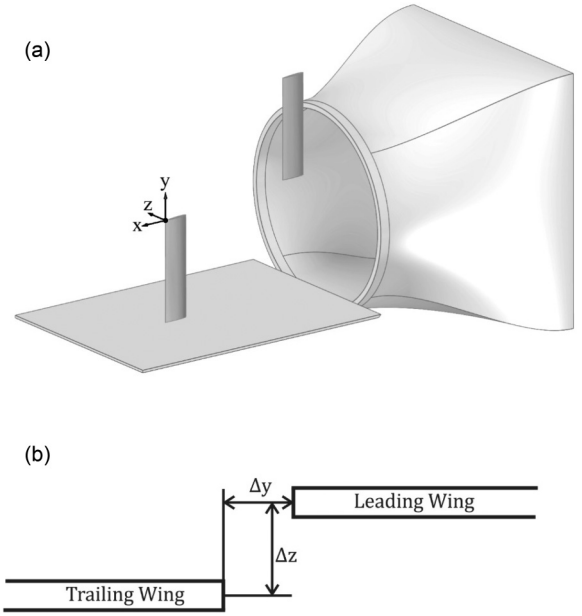

FIG. 1. (a) Experimental setup in the open section wind tunnel; (b) downstream view of both wings at 30% chord and definitions of wing separations.

at a sampling frequency of 3 Hz in the cross-correlation mode. The commercial software package Insight 4G and a Hart cross-correlation algorithm were used to analyze the images. For the image processing, an interrogation window size of 24 × 24 pixels was used, and velocity vectors were produced for further processing. The effective grid size was around 1 mm, which corresponds to a resolution of $0.01c$ by $0.01c$. Within the diameter of the viscous core of the vortices (defined by the maximum tangential velocity), there are typically 10 data points across the radial cut. The estimated uncertainty for velocity measurements was 2% of the freestream velocity U_∞.

The Gamma method [17] with a 5 × 5 pixels sized processing window was used to determine the location of vortex center for each instantaneous flow field. The variation of velocity magnitude as a function of distance from the center was calculated in eight azimuthal directions to find the location of the peak velocity magnitude, which is defined as the vortex core radius. The azimuthally averaged core radius was calculated for each instantaneous flow field. In addition, the vorticity in the core (at the center) and the circulation of the instantaneous vortex were recorded to calculate the ensemble-averaged quantities. As the interaction involved vortex pairs, locations of the instantaneous vortices and the distance between them were recorded for statistical analysis. The correlation coefficients between various variables were calculated. In addition, the probability of finding a vortex at a given location (in $0.02c \times 0.02c$ sized bins) was computed.

C. Hot-wire velocity measurements

As the PIV system did not have a high-frame rate, hot-wire measurements were performed with a TSI hot-wire probe and LabView software. The hot-wire probe was mounted on a long thin arm in the crossflow planes ($x/c = -1.05$ and $x/c = 0.05$) to capture the velocity near the vortex core. The hot-wire probe was placed on the periphery of the time-averaged vortex to minimize any intrusive effects due to the probe. This also means that the probe senses the irrotational fluctuations induced by the meandering. The probe's wire was placed parallel to the freestream so that it was most sensitive to the swirling velocity. Power spectral analysis was performed to obtain the vortex meandering

frequency. Sampling rate was set to 200 Hz. The freestream frequency spectrum did not reveal any peak. Therefore, any facility-induced perturbations were ruled out.

D. Force measurements

The force measurements were collected with a two-axis strain gauge type force balance and LabView software. The resonant frequency of the strain gauge force balance was above 20 Hz. The force balance was mounted under the splitter plate and was covered by a metal fairing. The gap between the root of the trailing wing and splitter plate was kept under 1 mm to minimize the leakage of the flow. Force data were collected at 200 Hz for a duration of 10 s at each location. This duration corresponds to more than 1,800 convective time units (c/U_∞) or 30 meandering periods. Then, the automatic traverse moved the leading wing on a whole grid of Δy and Δz locations. The resolution of the spatial grid was 10 mm, or $0.1c$.

E. Digital Image Correlation (DIC) deformation measurements

Digital image correlation measurements of the deformation of the flexible wing were carried out with a VIC 3D system. The system comprised a dual high-speed camera setup and accompanying lighting system. The flexible trailing wing was painted matt black and then speckled with random white spots, with spot diameter ranging from 0.5 to 3 mm. The wing deformation data were collected with a sampling rate of 50 Hz, and 2500 image pairs were stored for each case.

III. RESULTS AND DISCUSSION

A. Rigid trailing wing

Figure 2 presents the time-averaged vorticity patterns of the counter-rotating leading vortex and the trailing vortex of the downstream wing in a crossflow plane just downstream of the trailing wing ($x/c = 0.05$), for leading wing incidence $\alpha_{\mathrm{LW}} = 10^\circ$, and trailing wing incidence $\alpha_{\mathrm{TW}} = 5^\circ$. Each part in the figure corresponds to various combinations of the spanwise and normal separation distances. For $\Delta y/c = -0.3$ and $\Delta z/c = 0.3$ in Fig. 2(a), a relatively weak interaction is observed when the leading vortex is located above and inboard of the trailing wing tip. While the leading vortex has a nearly axisymmetric time-averaged shape, the trailing vortex system is weak due to the induced velocity of the leading vortex. Similar weak interaction can be observed for $\Delta y/c = 0.5$ and $\Delta z/c = 0$ in Fig. 2(b): in this case the time-averaged leading vortex is slightly squeezed at the top, suggesting that the presence of trailing wing has minor influence. For $\Delta y/c = 0$ and $\Delta z/c = -0.3$ in Fig. 2(c), no observable interaction is seen, as there is sufficient spatial separation between the vortices. The trailing vortex is also fully developed as the induced velocity of the incident vortex is smaller.

In contrast, intense interaction occurs when the trailing vortex is located just outboard and close to the trailing wing tip as shown in the right column. For $\Delta y/c = 0$ and $\Delta z/c = 0.2$ in Fig. 2(d), $\Delta z/c = 0.1$ in Fig. 2(e), $\Delta z/c = 0.0$ in Fig. 2(f), closely coupled vortex pairs with elongated shapes are formed. Deformation of the time-averaged leading vortex becomes significant as it is stretched upwards and inboard as the normal location of the leading wing is varied. Meanwhile, the trailing vortex is intensified in these cases by the upwash induced by the counter-rotating leading vortices.

These large deformations in the time-averaged vortex are due to the amplified meandering of the vortices. Figure 3 shows three instantaneous velocity fields for the case (e) in Fig. 2. Note that these three images were chosen as representative examples, as the PIV measurements are not time-resolved (the sampling frequency was 3 Hz). It is seen that the leading vortex exhibits large displacements in the crossflow plane. The location of the vortex dipole as well as the separation distance are highly time-dependent due to the meandering of the leading vortex. The largest induced velocity of the vortex pair is observed when vortices are closer to each other [Fig. 3(a)], displacing the pair in the inboard direction. Weaker interaction can be observed when the separation distance becomes larger

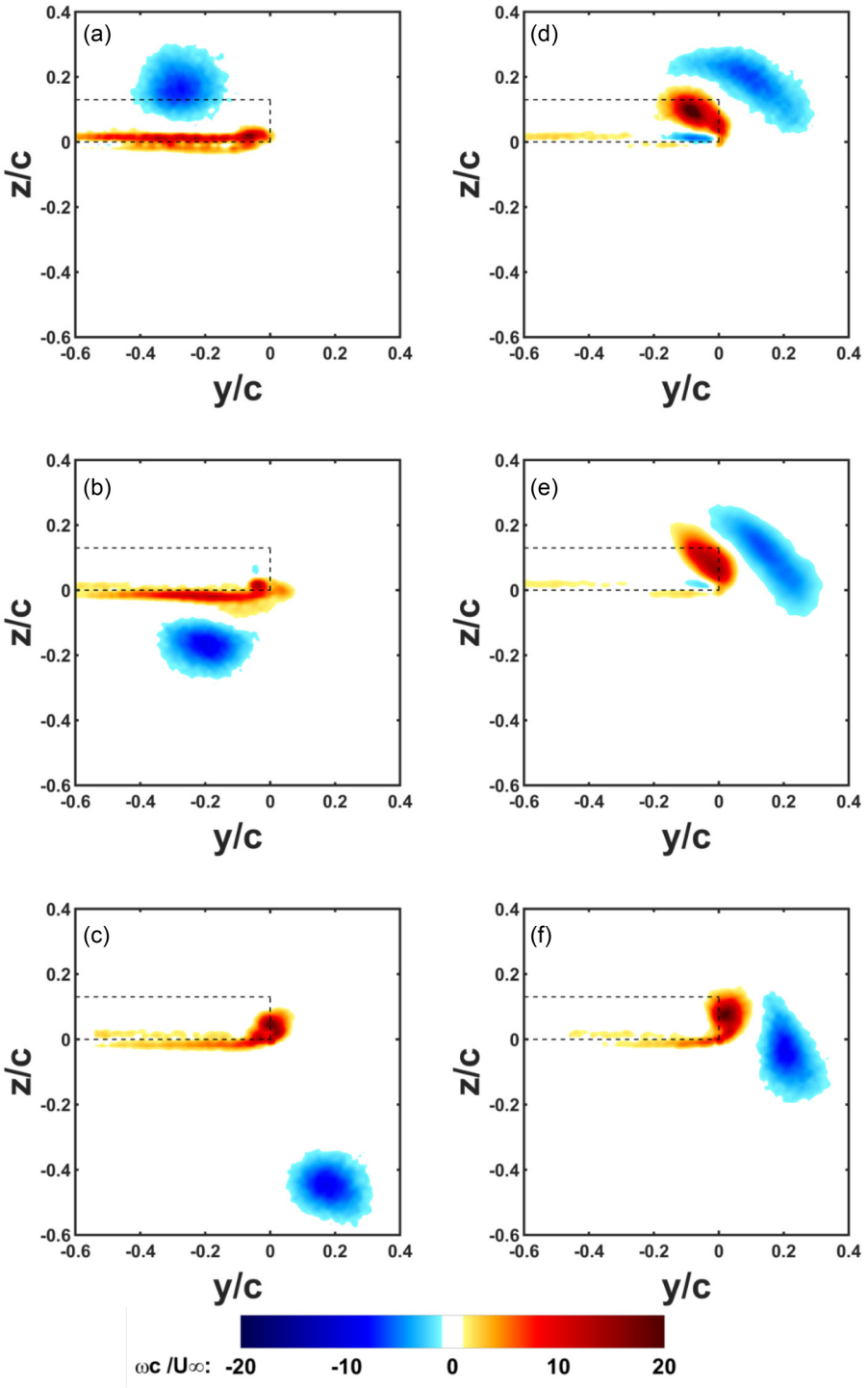

FIG. 2. Time-averaged vorticity patterns in the crossflow plane at $x/c = 0.05$, for $\alpha_{LW} = 10^\circ$, $\alpha_{TW} = 5^\circ$. (a) $\Delta y/c = -0.3$ and $\Delta z/c = 0.3$; (b) $\Delta y/c = -0.5$ and $\Delta z/c = 0$; (c) $\Delta y/c = 0$ and $\Delta z/c = -0.3$; (d) $\Delta y/c = 0$ and $\Delta z/c = 0.2$; (e) $\Delta y/c = 0$ and $\Delta z/c = 0.1$; (f) $\Delta y/c = 0$ and $\Delta z/c = 0$.

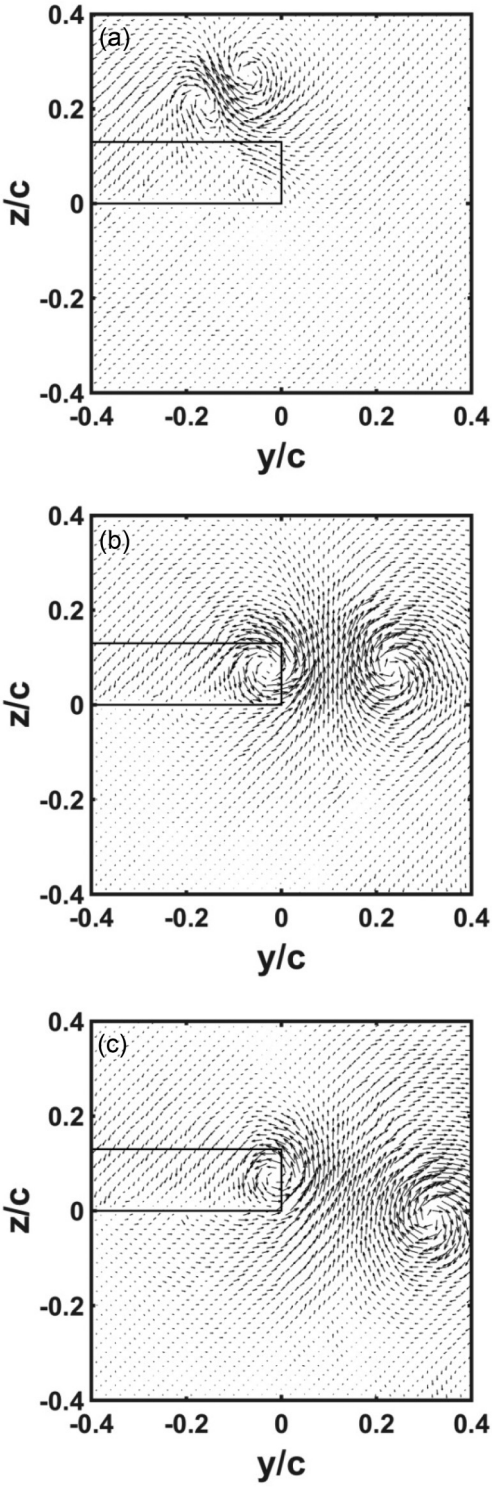

FIG. 3. Three instantaneous velocity fields in the crossflow plane at $x/c = 0.05$, for $\alpha_{LW} = 10^{\circ}$, $\alpha_{TW} = 5^{\circ}$, $\Delta y/c = 0$, and $\Delta z/c = 0.1$.

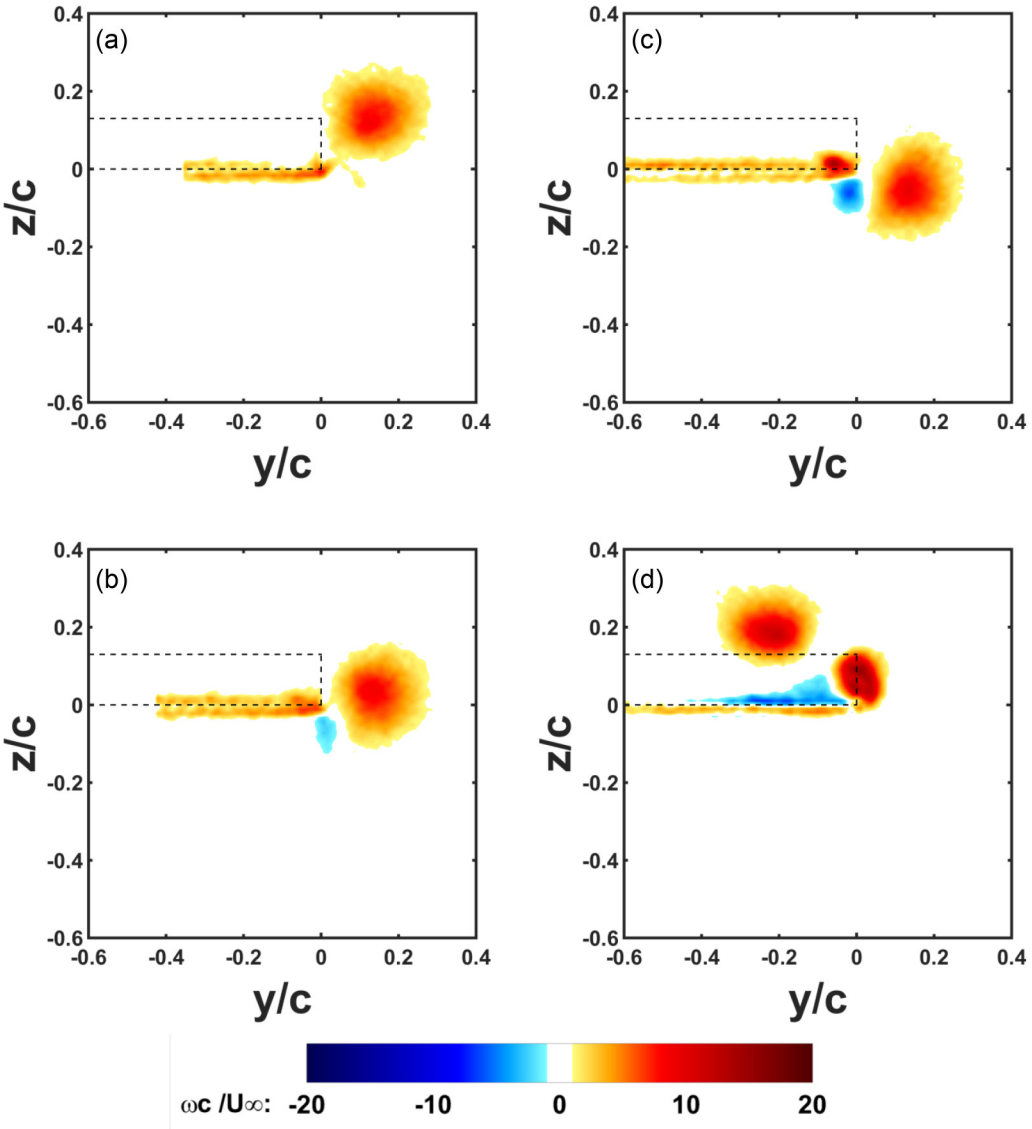

FIG. 4. Time-averaged vorticity patterns in the crossflow plane at $x/c = 0.05$, for $\alpha_{LW} = -10^\circ$, $\alpha_{TW} = 5^\circ$. (a) $\Delta y/c = 0$ and $\Delta z/c = -0.1$; (b) $\Delta y/c = 0$ and $\Delta z/c = -0.2$; (c) $\Delta y/c = 0$ and $\Delta z/c = -0.3$; (d) $\Delta y/c = -0.4$ and $\Delta z/c = 0$.

[Fig. 3(c)], resulting in the leading vortex being displaced outboard and the trailing vortex returning near the wing tip.

The time-averaged vorticity fields of the co-rotating leading and trailing vortices are presented in Fig. 4, for the same crossflow plane, $x/c = 0.05$, and $\alpha_{LW} = -10^\circ$, $\alpha_{TW} = 5^\circ$. The trailing vortex is suppressed when the leading vortex is located outboard of the trailing wing tip due to its downwash [Figs. 4(a)–4(c)]. In spite of the proximity of the leading vortex to the wing tip, there is not much deformation in the time-averaged vorticity of the leading vortex. As the vertical location of the leading wing is decreased, stronger downwash even causes the formation of a clockwise tip vortex on the bottom surface of the trailing wing tip [Fig. 4(c)]. However, when the leading vortex is located inboard and above the trailing wing tip [Fig. 4(d)], the upwash strengthens the trailing vortex, while

the opposite sign of vorticity is formed on the surface of the wing between the vortex pair. Again, there is not much deformation of the time-averaged leading vortex, which implies the absence of amplified meandering for the interaction of co-rotating leading vortices with downstream wings.

It is possible that vortex meandering depends on the relative strengths of the leading vortex and trailing vortex. To vary the ratio of the strengths (circulations), we carried out experiments with the trailing wing set at the same incidence as the upstream wing. Figure 5 exhibits vorticity patterns of both counter-rotating (left column) and co-rotating (right column) vortices for the trailing wing angle of attack, $\alpha_{TW} = 10^\circ$. Elongation of the time-averaged vortex is visible for the close interaction of the counter-rotating vortex [Figs. 5(a) and 5(b)], where the meandering of the leading vortex was greatly spread along the vicinity of the trailing vortex. There is less meandering in Fig. 5(c), where the leading vortex is a little further away from the tip. These observations are similar to those for the lower angle of attack of the trailing wing. Similarly, for the interactions of the co-rotating vortices (shown in the right column), there is no evidence of increased meandering. Merging of the co-rotating vortices can be observed in Figs. 5(d) and 5(e). A weak interaction is observed when the separation distance is large [Fig. 5(f)].

We also carried out experiments for weaker leading vortices by decreasing the angle of attack of the leading wing to $\alpha_{LW} = 5^\circ$, as the dimensionless strength ($\Gamma/U_\infty c$) might also be important. With the weaker leading vortices (Fig. 6), the trailing vortex experiences qualitatively similar elongation for close interactions. In summary, the vortex deformation in the time-averaged pattern due to the meandering vortices is generic to the interaction of the counter-rotating vortices, when the upstream vortex is near the tip of the downstream wing. For these close interactions, the formation of a pair of counter-rotating vortices and the resulting induced velocity of the pair are essential characteristics. In contrast, co-rotating vortices do not exhibit increased meandering when they interact with the downstream wing.

The increased meandering of the upstream vortices as they interact with the downstream wing may cause increased unsteady forces on the wing. Figure 7 presents the percent change in the mean lift force and the root-mean square lift of the trailing wing with respect to the baseline case (no upstream vortex) as a function of wing separation for $\alpha_{LW} = 10^\circ$, $\alpha_{TW} = 5^\circ$. The wing spanwise separation $\Delta y/c$ ranged from -1 to 0.6 and the normal separation $\Delta z/c$ ranged from -0.8 to 1.2. The leading wing was found to have a positive influence on the lift coefficient of the trailing wing, with a peak increase of 20% at $\Delta y/c = -0.2$ and $\Delta z/c = 0.2$ (slightly inboard and above the trailing wing tip). However, the highest root-mean square lift coefficient occurs at slightly outboard and above the trailing wing-tip location, where a close vortex pair is formed. The corresponding flow fields for selected cases can be seen in Fig. 2. Both Figs. 2(d) and 2(e) produce the largest unsteady lift as seen in Fig. 7. It is interesting that the unsteady vortex pairs cause larger lift fluctuations than the direct impingement on the wing at inboard locations.

For selected cases of close interaction of the counter-rotating vortices, PIV measurements in various crossflow planes were carried out and are shown in Fig. 8. In these cases, the strength of the leading wing vortex was kept the same ($\alpha_{LW} = 10^\circ$) and the trailing-wing incidence or vortex location were varied. All three plots of three-dimensional views of the time-averaged vorticity patterns (in the crossflow planes from $x/c = -1.05$ to 0.05) shown in Fig. 8 reveal the growth of the meandering amplitude of the leading vortex as it travels downstream along the trailing wing. For the cases shown in Figs. 8(a) and 8(b), the deformation of the leading vortex pattern accelerates just before the mid-chord location of the trailing wing, while in Fig. 8(c), with slight change in the spanwise separation distance to $\Delta y/c = -0.1$, the deformation of the leading vortex pattern starts much earlier. For the same location of the leading vortex, but with different angles of attack of the trailing wing [compare Figs. 8(a) and 8(b)], the elongation of the leading vortex appears larger and grows faster when the trailing vortex is stronger. These measurements at different planes are not simultaneously taken and the three-dimensional trajectory of the instantaneous vortex cannot be deduced. However, it is very likely that the streamwise wavelength of the meandering is much larger than the chord length of the airfoil. Further evidence will be discussed below.

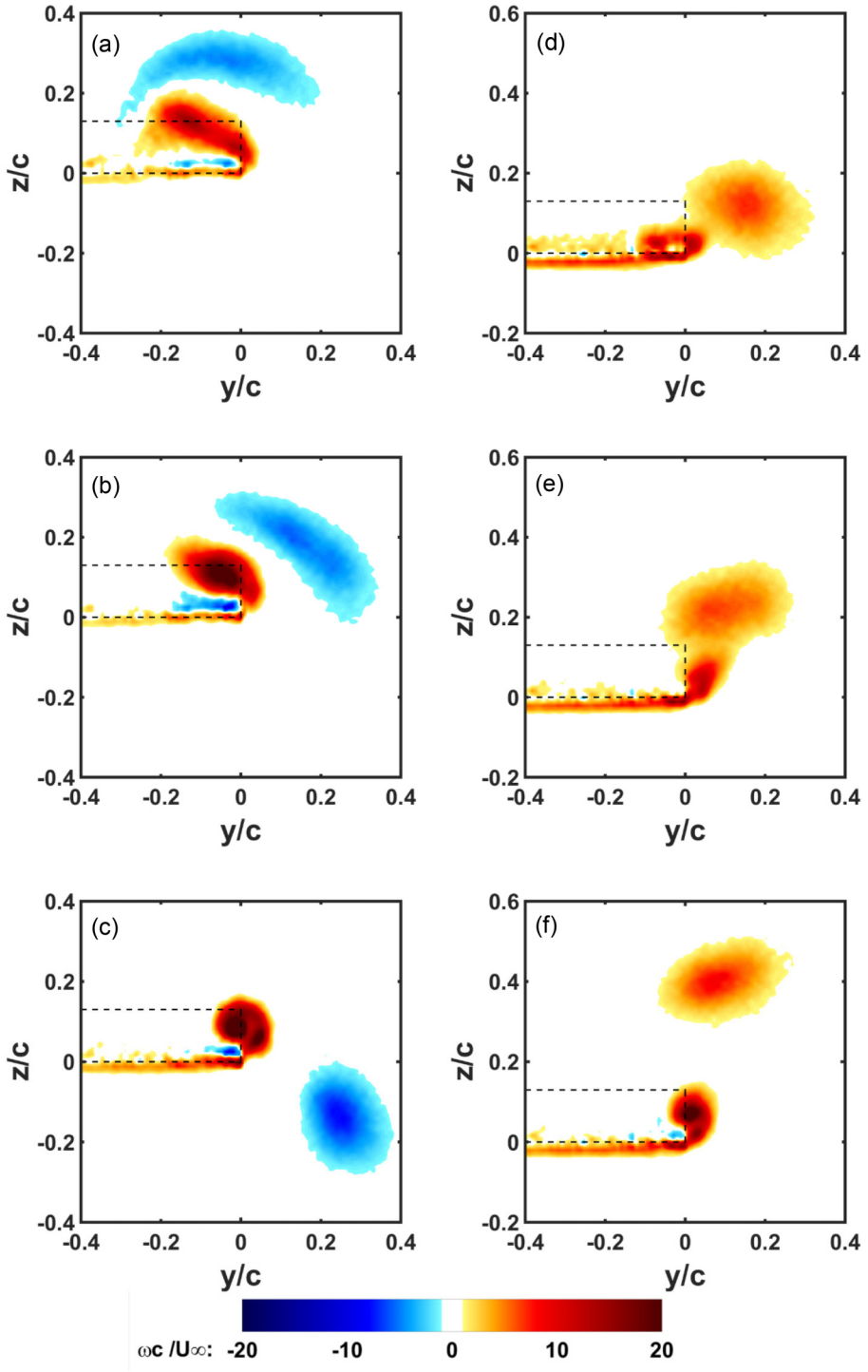

FIG. 5. Time-averaged vorticity patterns in the crossflow plane at $x/c = 0.05$, for $\alpha_{TW} = 10^\circ$. (a) $\alpha_{LW} = 10^\circ$, $\Delta y/c = -0.1$, and $\Delta z/c = 0.2$; (b) $\alpha_{LW} = 10^\circ$, $\Delta y/c = 0$, and $\Delta z/c = 0.1$; (c) $\alpha_{LW} = 10^\circ$, $\Delta y/c = 0$, and $\Delta z/c = -0.1$; (d) $\alpha_{LW} = -10^\circ$, $\Delta y/c = 0$, and $\Delta z/c = -0.25$; (e) $\alpha_{LW} = -10^\circ$, $\Delta y/c = 0$, and $\Delta z/c = -0.1$; (f) $\alpha_{LW} = -10^\circ$, $\Delta y/c = 0$, and $\Delta z/c = 0.1$.

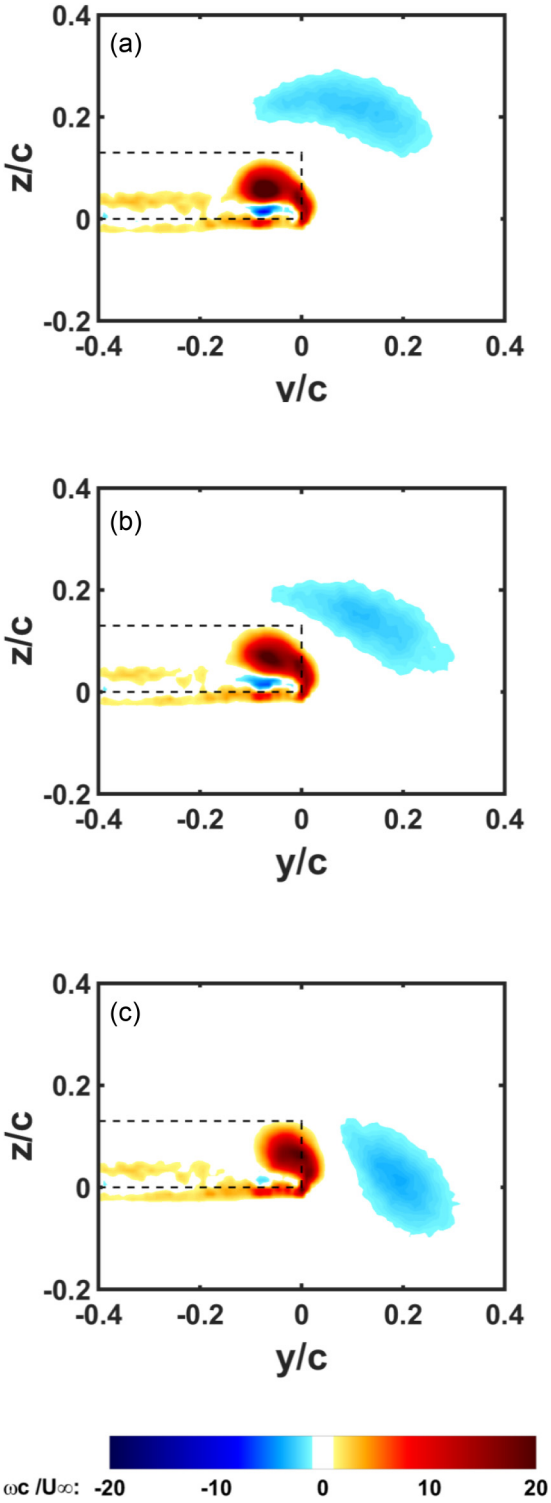

FIG. 6. Time-averaged vorticity patterns in the crossflow plane at $x/c = 0.05$, for $\alpha_{LW} = 5^\circ$, $\alpha_{TW} = 5^\circ$. (a) $\Delta y/c = 0$ and $\Delta z/c = 0.15$; (b) $\Delta y/c = 0$ and $\Delta z/c = 0.05$; (c) $\Delta y/c = 0$ and $\Delta z/c = -0.05$.

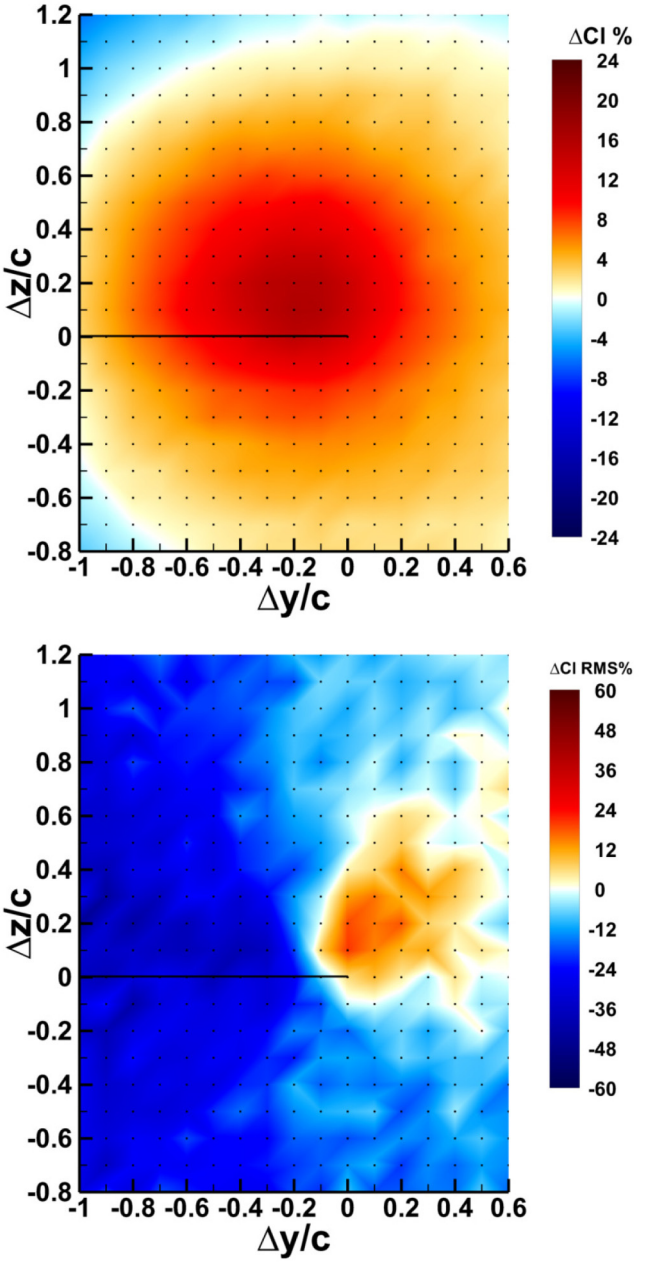

FIG. 7. Percent change in time-averaged lift (top) and in root-mean square lift (bottom) as a function of wing separations in the spanwise and normal directions, $\alpha_{\mathrm{LW}} = 10^{\circ}$, $\alpha_{\mathrm{TW}} = 5^{\circ}$. The baseline case is the trailing wing in the freestream. The horizontal solid line represents the trailing-edge of the wing.

Even in the absence of a downstream wing, it is well known that there is meandering of isolated trailing vortices. Although the flow physics is much debated [18], there is recent evidence that it may originate from an instability of the vortex filament [19,20]. This instability is in the form of first helical mode, with a very large wavelength (on the order of 10^2 to 10^3 times the vortex core radius) and correspondingly low frequency of meandering. It was observed in various experiments on tip

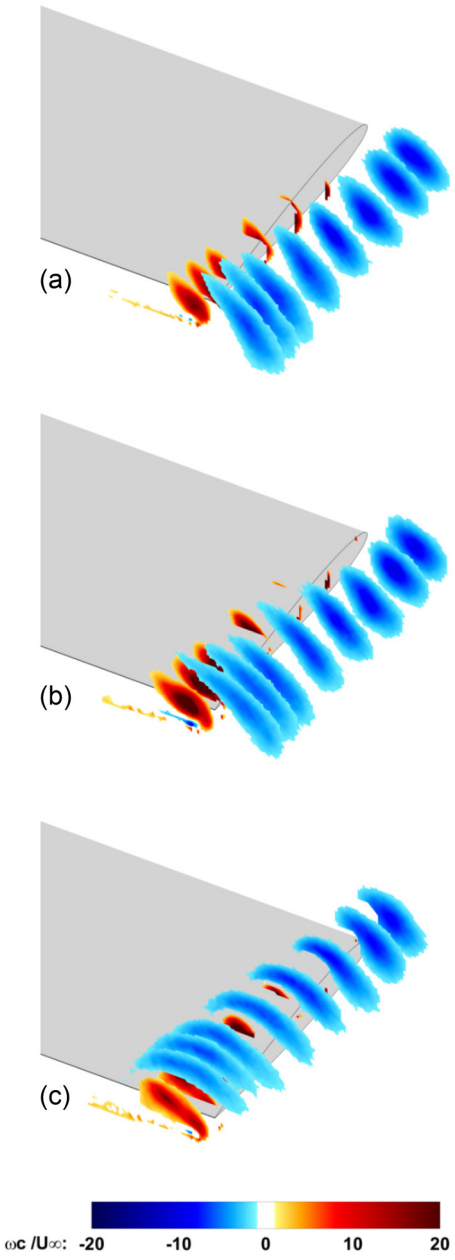

FIG. 8. Three-dimensional view of time-averaged vorticity patterns in the crossflow planes from $x/c = -1.05$ to 0.05; (a) $\alpha_{LW} = 10^\circ$, $\alpha_{TW} = 5^\circ$, $\Delta y/c = 0$, and $\Delta z/c = 0.1$; (b) $\alpha_{LW} = 10^\circ$, $\alpha_{TW} = 10^\circ$, $\Delta y/c = 0$, and $\Delta z/c = 0.1$; (c) $\alpha_{LW} = 10^\circ$, $\alpha_{TW} = 10^\circ$, $\Delta y/c = -0.1$, and $\Delta z/c = 0.2$.

vortices [12,13,20–22] as well as leading-edge vortices [23,24]. Figure 9 presents the time-averaged vorticity pattern and flow structures of the dominant proper orthogonal decompostion (POD) modes in the crossflow plane at $x/c = 0.05$ for $\alpha_{LW} = 10^\circ$ in the absence of the trailing wing. Slightly elongated mean vorticity due to the meandering results in a larger apparent core radius than that of the instantaneous vortex. Table I shows that the ensemble-average of instantaneous radius of

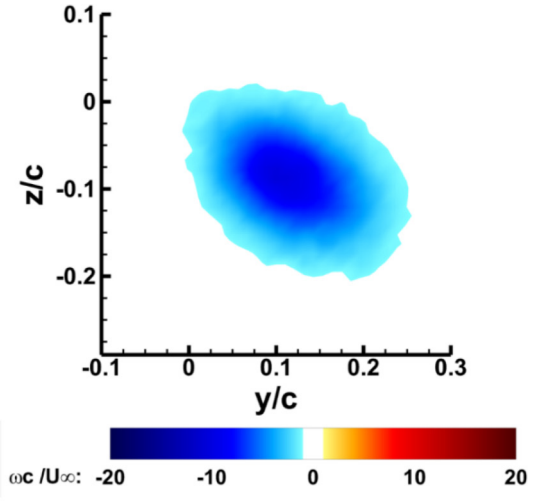

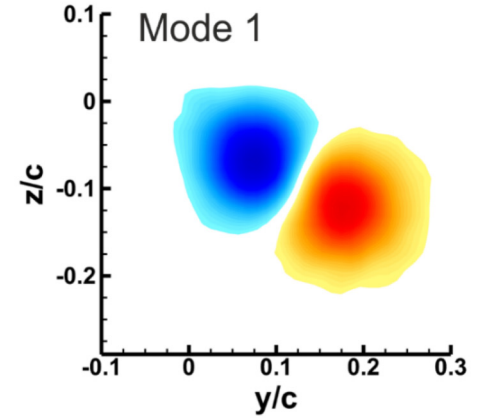

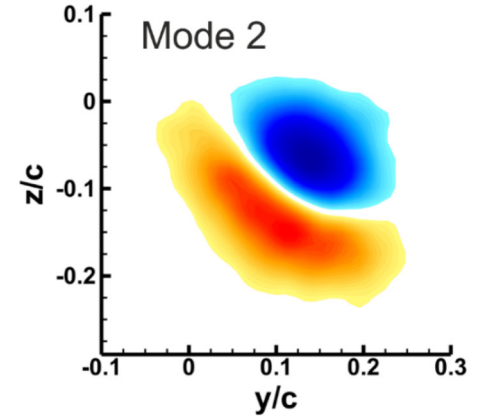

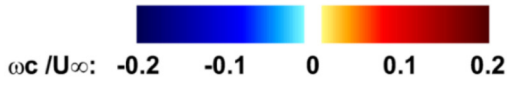

FIG. 9. Time-averaged vorticity patterns and flow structures of the first two POD modes in the crossflow plane at $x/c = 0.05$, leading vortex alone, $\alpha_{LW} = 10^{\circ}$.

TABLE I. Ensemble average and standard deviation of core location, core radius, absolute dimensionless vorticity at the core center, and dimensionless circulation for the leading vortex (LV) and trailing vortex (TV) alone and in the interaction with the wing. $x/c = 0.05$, $\alpha_{LW} = 10^\circ$, $\alpha_{TW} = 5^\circ$, $\Delta y/c = 0, \Delta z/c = 0.1$.

	y/c	z/c	a/c	Γ^*	${\omega_c}^*$
LV alone	0.15 ± 0.07	-0.13 ± 0.05	0.05 ± 0.01	0.20 ± 0.01	42 ± 9
LV interaction	0.16 ± 0.08	0.11 ± 0.09	0.06 ± 0.01	0.20 ± 0.02	31 ± 6
TV alone	-0.04 ± 0.03	0.03 ± 0.01	0.05 ± 0.01	0.18 ± 0.01	32 ± 9
TV interaction	-0.05 ± 0.04	0.11 ± 0.03	0.06 ± 0.01	0.19 ± 0.02	33 ± 10

the leading vortex is $a_{LV}/c = 0.05$. The method of snapshot [25] was used and the POD analysis was performed by using MATLAB codes developed based on the technique proposed by Chen *et al.* [26]. In the first (most energetic) mode (37% of the total energy), a vortex pair centered on the time averaged vortex is observed, representing nearly vertical displacements of the vortex. A similar vortex pair is also observed in the second mode (16% of the total energy), which is also centered on the time-averaged vortex with its main direction nearly perpendicular to the first mode. A linear combination of these eigen modes provides displacements of the vortex core, which can be characterized as azimuthal wavenumber of $m = 1$. Similar first helical mode was observed in previous experiments on tip vortices [12,13,20–22] and delta wing vortices [23,24].

In Fig. 10, the frequency spectrum of the velocity fluctuations near the core of the leading vortex alone (in the absence of a downstream wing) is shown. The hot-wire probe is located at $y/c = 0.2$ and $z/c = 0$. The spectrum indicates a peak frequency of about 2.8 Hz, corresponding to the Strouhal number (based on the chord length) of $St_c = 0.015$. This frequency is believed to be the result of the first helical mode, representing the frequency of the dominant meandering behavior, and is consistent with previous observations. If it is assumed that this helical wave propagates with the freestream velocity, we obtain a wavelength ratio of $\lambda/c \approx 67$ or $\lambda/a \approx 1{,}300$. Various previous experiments estimated that the dominant wavelength of meandering is on the order of 10^2 to 10^3 times the vortex core radius as summarized by Chen *et al.* [12]. For example, this ratio is about 200 (in Ref. [20]), 610 (in Ref. [12]) and 2,000 (in Ref. [27]). Although most of the estimates are based on the frequency spectra in a streamwise station, they are in good agreement with the direct estimate from

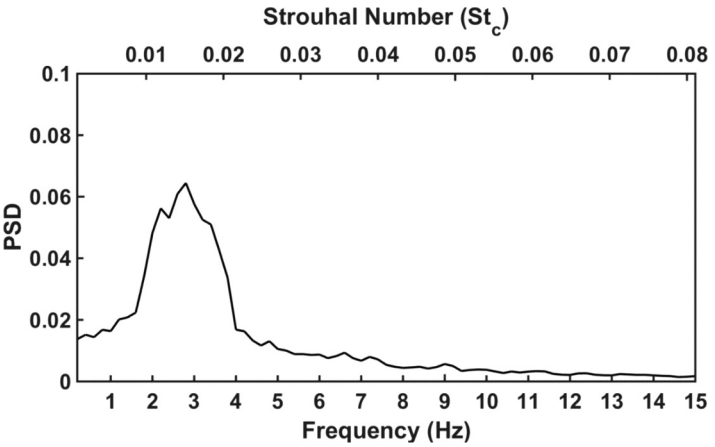

FIG. 10. Frequency spectra of velocity near the core of the isolated vortex at $x/c = 0.05$, $\alpha_{LW} = 10^\circ$, hot-wire probe location $y/c = 0.2$, $z/c = 0$.

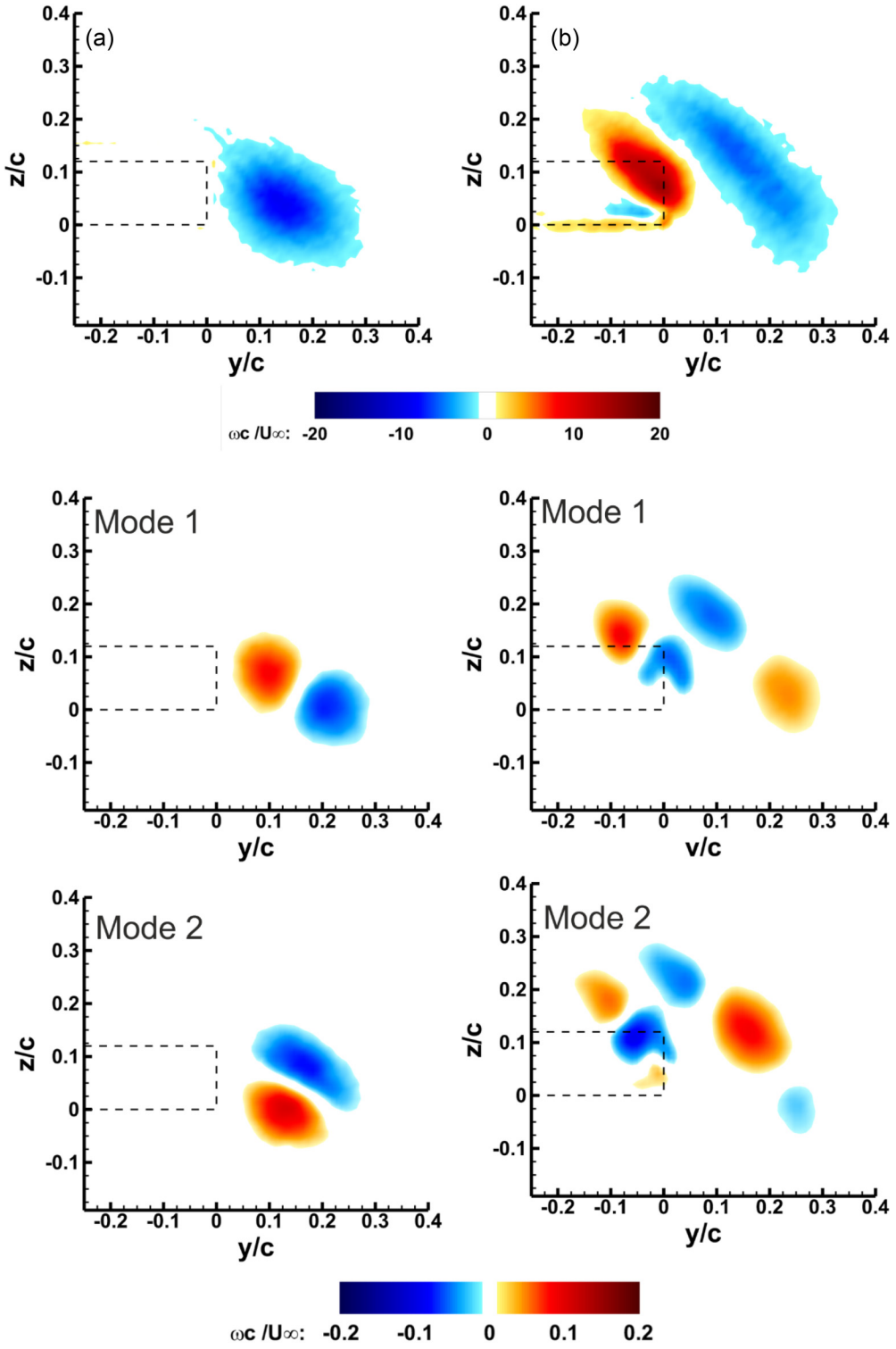

FIG. 11. Time-averaged vorticity patterns and flow structures of the first two POD modes in the crossflow planes (a) $x/c = -1.05$ (left), (b) $x/c = 0.05$ (right). $\alpha_{\mathrm{LW}} = 10^{\circ}$, $\alpha_{\mathrm{TW}} = 5^{\circ}$, $\Delta y/c = 0$, and $\Delta z/c = 0.1$.

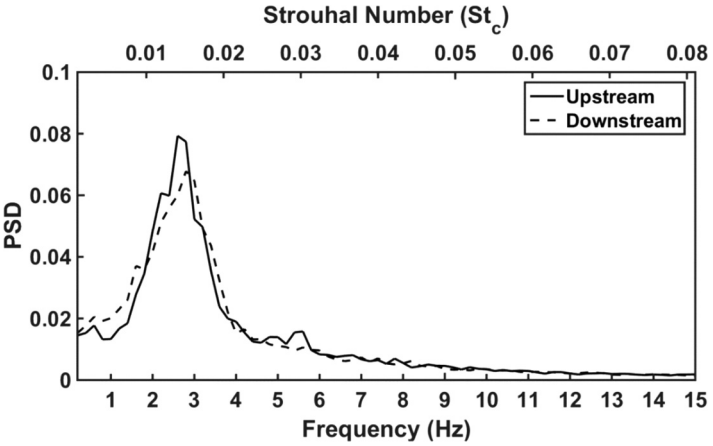

FIG. 12. Frequency spectra of velocity near the vortex core in the planes at $x/c = -1.05$ (upstream) and 0.05 (downstream), for $\alpha_{LW} = 10^\circ$, $\alpha_{TW} = 5^\circ$, $\Delta y/c = 0$, and $\Delta z/c = 0.1$. Hot-wire probe location $y/c = 0.2$, $z/c = 0$.

the volumetric measurements and the three-dimensional POD modes [12]. The inviscid mechanism of infinite growth in the limit of infinitely large wavelengths [19,28,29] may provide the theoretical support for these observations.

Figure 11 presents the time-averaged vorticity patterns and flow structures of the dominant POD modes in the crossflow planes at $x/c = -1.05$ and $x/c = 0.05$ for the close interaction case, $\alpha_{LW} = 10^\circ$, $\alpha_{TW} = 5^\circ$, $\Delta y/c = 0$, and $\Delta z/c = 0.1$. (This case is shown in Figs. 2(e) and 3.) Just upstream of the wing [Fig. 11(a)], the two most energetic modes (36% and 16% of the total energy) of the leading vortex remain very similar to those of the leading vortex alone. Downstream of the trailing edge [Fig. 11(b)], two vortex pairs each belonging to the leading and trailing vortices can be observed in the most energetic modes. The locations of the vortex pairs representing the leading vortex are different in mode 1 (42% of the total energy) and mode 2 (17% of the total energy), and reflect the large meandering motion. These mode shapes might also indicate an effect of increased variation of the strength (see also Table I). While the variations in the core size remain roughly the same, the largest variations appear to be in the location of the vortex (meandering). In fact, the mode 2 in the interaction case seems to be a translation of the mode 1 along the vortex trajectory within the region of the time-averaged vorticity. That is why we believe that the main effect is due to the large meandering motion.

The frequency spectra of the velocity fluctuations near the leading vortex in this case are displayed in Fig. 12. The hot-wire probe was located at $y/c = 0.2$ and $z/c = 0$ in both crossflow planes [$x/c = -1.05$ (upstream) and $x/c = 0.05$ (downstream)]. Identical peak frequencies in both planes are noted. Also, this is the same frequency as in the case of the leading vortex alone. Hence, we conclude that large amplitude meandering takes place at the same natural frequency of meandering of the isolated vortex. As the dominant frequency of meandering is around $f \approx 2.8$ to 3.0 Hz, we used a sampling rate of 3 Hz in our PIV measurements. Some sample instantaneous flow fields were shown in Fig. 3. It is obvious that the flow is not perfectly periodic, but only quasiperiodic in nature. Therefore, phase-locked measurements are not possible. As we do not have a high-frame PIV system, we could only conduct a statistical analysis of randomly captured flow fields. This is discussed next.

Figure 13 presents plots of the probability of instantaneous location of the leading wing vortex for this close interaction case (see also Figs. 2(e) and 3), in the crossflow planes $x/c = -1.05$ and $x/c = 0.05$. In the upstream plane, the probability of vortex core location formed a nearly circular pattern with peak probability of 22% at the center, and gradually decreased further out. In the downstream plane, the meandering distribution became a highly diagonally stretched pattern, with

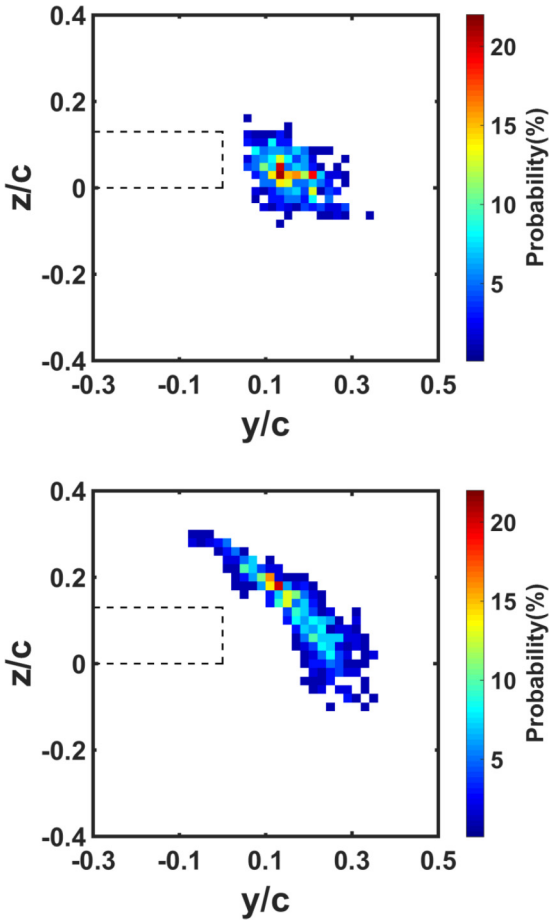

FIG. 13. Probability of instantaneous location of the leading vortex in the crossflow plane at $x/c = -1.05$ (top) and $x/c = 0.05$ (bottom), $\alpha_{\mathrm{LW}} = 10^{\circ}$, $\alpha_{\mathrm{TW}} = 5^{\circ}$, $\Delta y/c = 0$, and $\Delta z/c = 0.1$.

higher probability near the center, and decreased further out. The high probability ($>10\%$) locations form a narrow, nearly linear line.

The time series of both leading and trailing vortex core locations in the downstream plane $x/c = 0.05$ are plotted in Fig. 14. It is obvious the leading vortex (in red) experienced significantly larger displacements, compared to those of the trailing vortex (in black). A positive correlation can be observed between the locations of vortices both in the spanwise and normal directions. The ensemble-average and root-mean square values of the vortex core location, vortex core radius, absolute circulation ($\Gamma^* = \Gamma/U_\infty \mathrm{c}$), and vorticity in the core center ($\omega_c^* = \omega_c c/U_\infty$) for this interaction case and the vortex alone case are presented for both vortices in Table I. The mean spanwise location of the leading vortex has not seen significant change due to the interaction; however, the mean normal location was significantly influenced by the presence of the trailing wing. Both spanwise and normal locations have seen increase in their root-mean square values with the interaction. The core radius of the vortex increased from $0.05c$ to $0.06c$ after the interaction. Note that the mean circulation of the leading vortex does not differ when the trailing wing is absent or present, while there is some decrease of the core vorticity that is accompanied by the expansion of the core radius with the interaction.

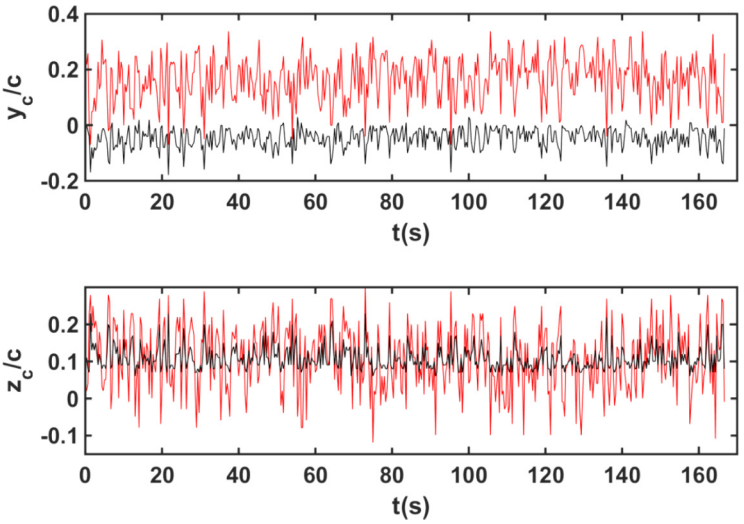

FIG. 14. Time histories of spanwise and normal locations of the leading (red) and trailing (black) vortices in the crossflow plane at $x/c = 0.05$. $\alpha_{LW} = 10^\circ$, $\alpha_{TW} = 5^\circ$, $\Delta y/c = 0$, and $\Delta z/c = 0.1$.

Table II shows the correlation coefficients between the vortex core locations, vortex core radius, absolute circulation, vorticity in the core center, and separation distance between the leading and trailing vortices. It is seen that leading and trailing vortex locations, both in the spanwise and normal directions, have significant correlation. The spanwise location of the leading vortex y_{LV}/c has a positive correlation with the spanwise location of the trailing vortex and negative correlation with the normal location of the trailing vortex. There is also a very high correlation of the spanwise coordinate of the leading vortex with the separation distance b between the vortices. The core radius of the leading vortex a_{LV}/c has almost no correlation with the vortex meandering; however, there is some correlation of the core vorticity with the vortex displacement. The core radius of the trailing vortex a_{TV}/c has a correlation coefficient of -0.49 with its core vorticity, which suggests decreasing peak vorticity with the expansion of the core that occurs when the vortex dipole separation increases. The circulation of the trailing vortex $\Gamma_{TV}{}^*$ has higher correlation with meandering, in particular with its normal location. A strong correlation can be observed between the core vorticity and the location

TABLE II. Correlation coefficients between core locations, core radius, absolute circulation, vorticity at the core center, and distance between the leading and trailing vortices. $x/c = 0.05$, $\alpha_{LW} = 10^\circ$, $\alpha_{TW} = 5^\circ$, $\Delta y/c = 0, \Delta z/c = 0.1$.

	y_{TV}/c	z_{LV}/c	z_{TV}/c	a_{LV}/c	a_{TV}/c	Γ^*_{LV}	Γ^*_{TV}	$\omega^*_{c\,LV}$	$\omega^*_{c\,TV}$	b/c
y_{LV}/c	0.86	−0.88	−0.86	0.05	0.27	0.35	−0.35	0.54	−0.62	0.92
y_{TV}/c		−0.90	−0.86	−0.05	0.26	0.19	−0.41	0.46	−0.64	0.63
z_{LV}/c			0.83	0.15	−0.17	−0.20	0.51	−0.53	0.62	−0.76
z_{TV}/c				0.00	−0.25	−0.25	0.26	−0.51	0.59	−0.74
a_{LV}/c					0.03	0.20	0.19	−0.24	0.01	0.06
a_{TV}/c						0.07	0.04	0.10	−0.49	0.21
Γ^*_{LV}							0.17	0.25	−0.02	0.38
Γ^*_{TV}								−0.22	0.37	−0.32
$\omega^*_{c\,LV}$									−0.28	0.48
$\omega^*_{c\,TV}$										−0.48

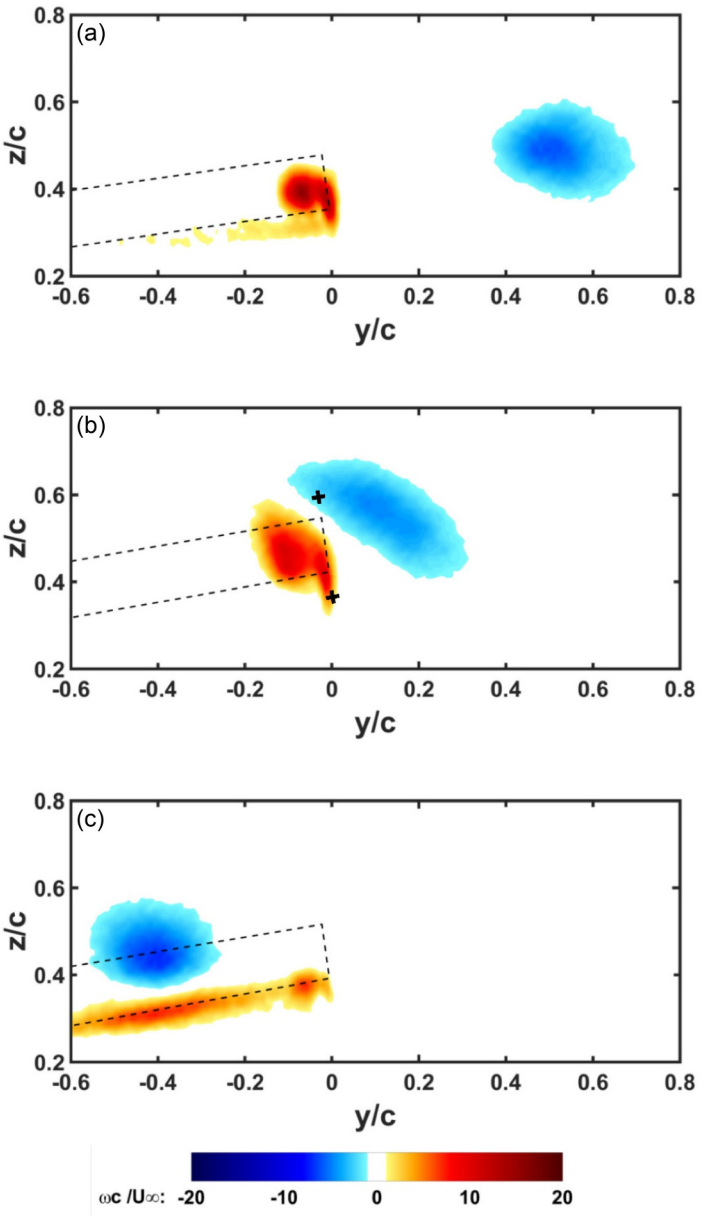

FIG. 15. Time-averaged vorticity patterns in the crossflow plane at $x/c = 0.05$, for $\alpha_{\mathrm{LW}} = 10^{\circ}$, $\alpha_{\mathrm{TW}} = 5^{\circ}$, flexible trailing wing: (a) $\Delta y/c = 0.4$ and $\Delta z/c = 0.6$; (b) $\Delta y/c = 0$ and $\Delta z/c = 0.6$; (c) $\Delta y/c = -0.4$ and $\Delta z/c = 0.6$. Dashed lines indicate mean location of the trailing wing; "+" signs in (b) indicate the standard deviation of deformation.

of the trailing vortex. In summary, there is larger meandering of the leading vortex, which causes highly correlated variations in the structure of the trailing vortex.

B. Flexible trailing wing

Returning to the earlier observation that amplified meandering occurs at the natural frequency of the vortex instability and the flow is quasiperiodic, one interesting aspect is the interaction of

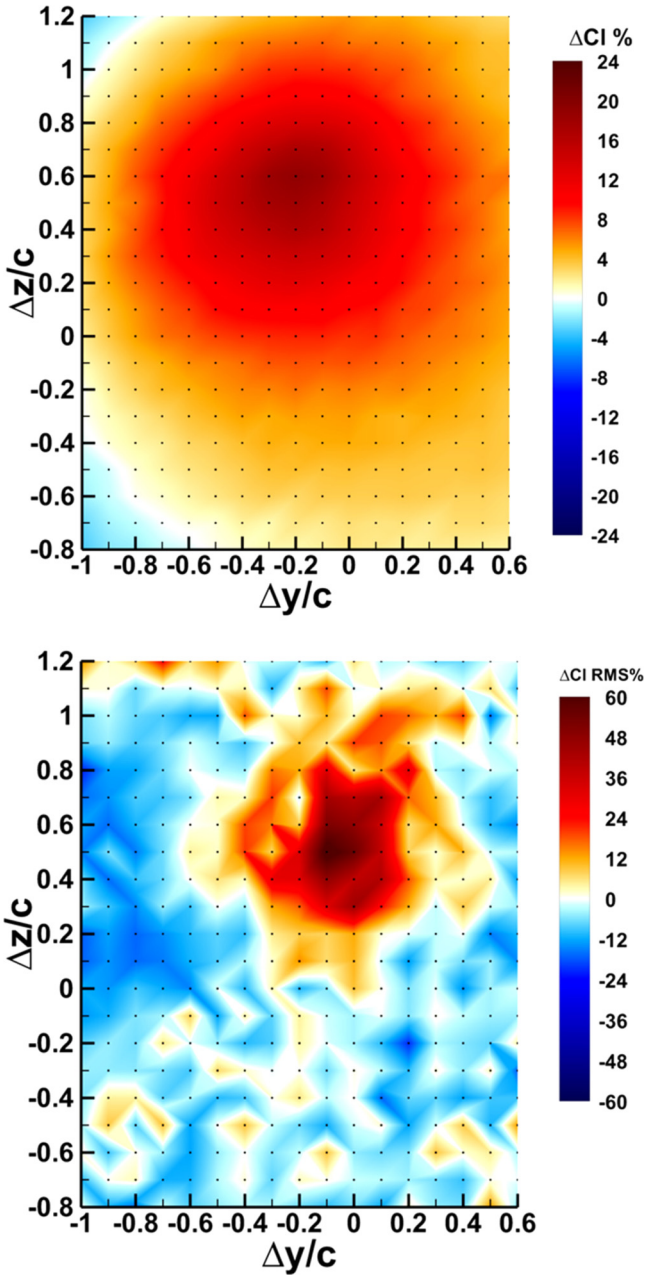

FIG. 16. Percent change in time-averaged lift (top) and in root-mean square lift (bottom) of the flexible wing as a function of wing separations in the spanwise and normal directions, $\alpha_{LW} = 10^{\circ}$, $\alpha_{TW} = 5^{\circ}$. The baseline case is the trailing wing in the freestream.

the incident vortices with a flexible downstream wing. To study this, we designed a flexible wing with a natural frequency of bending oscillations closely matching the natural frequency of the vortex meandering. Deformation measurements showed that the natural frequency in the bending mode was about 3.5 Hz, which is reasonably close to the meandering frequency (about 3 Hz) of the incident vortex. Time-averaged vorticity patterns for the flexible trailing wing in the crossflow plane

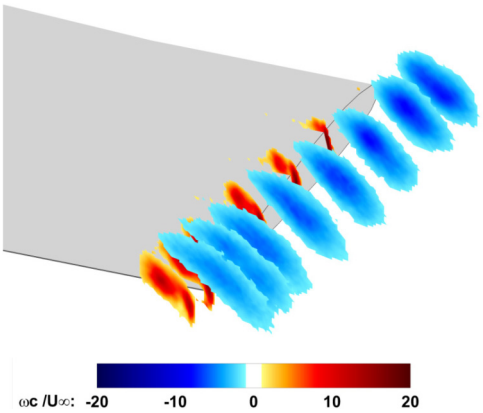

FIG. 17. Three-dimensional view of time-averaged vorticity patterns in the crossflow planes from $x/c = -1.05$ to 0.05; $\alpha_{LW} = 10°$, $\alpha_{TW} = 5°$, $\Delta y/c = 0$, and $\Delta z/c = 0.6$, flexible trailing wing.

at $x/c = 0.05$ are illustrated in Fig. 15 for $\alpha_{LW} = 10°$, $\alpha_{TW} = 5°$, (a) $\Delta y/c = 0.4$ and $\Delta z/c = 0.6$; (b) $\Delta y/c = 0$ and $\Delta z/c = 0.6$; (c) $\Delta y/c = -0.4$ and $\Delta z/c = 0.6$. Dashed lines indicate the time-averaged location of the trailing wing. It is seen that the flexible wing exhibits similar behavior to the rigid wing: weak to no interaction is observed if the separation distance is large as in Figs. 15(a) and 15(c), and a strong interaction with elongated (time-averaged) leading and trailing vortices as in Fig. 15(b). It is also seen that the mean wing deflection varies depending on the location of the leading vortex as the mean loading on the wing is affected. For Fig. 15(b), we carried out detailed deformation measurements. For this case we added the standard deviation of the wing-tip bending deformation to Fig. 15(b) with "+" signs. Figure 16 presents the percent change in the mean lift force and the root-mean square lift of the trailing wing with respect to the baseline case (no upstream vortex) as a function of wing separation for $\alpha_{LW} = 10°$ and $\alpha_{TW} = 5°$. The time-averaged location of the wing is not shown as it varies for each combination of $\Delta y/c$ and $\Delta z/c$, and it has only been measured for a few selected cases. There is a peak increase near $\Delta y/c = -0.2$ and $\Delta z/c = 0.6$. The mean deformation measurements for selected cases (not shown here) and various separation distances around the location of the mean lift peak in Fig. 16 indicate that there is a monotonic relationship between the mean deformation and the mean lift. The largest mean deflection occurs when the mean lift is largest.

Figure 16 also shows that the highest root-mean square lift increase occurs slightly outboard. The case presented in Fig. 15(b) is representative of the high-lift and high-unsteady-lift configuration, which reveals the formation of the vortex dipole as in the case of the rigid wings. This configuration ($\Delta y/c = 0$ and $\Delta z/c = 0.6$) has been studied by means of additional PIV measurments in various crossflow planes. The three-dimensional view of the time-averaged vorticity patterns for this case is presented in Fig. 17, between $x/c = -1.05$ to 0.05, for $\alpha_{LW} = 10°$, $\alpha_{TW} = 5°$, $\Delta y/c = 0$, and $\Delta z/c = 0.6$. It appears that the leading vortex starts to stretch and become elongated at a more upstream location compared to the rigid wing cases, possibly due to the influence of the large oscillation amplitude of the trailing wing tip. The unsteady deformation of the wing was mostly in the bending mode. The torsional deformation amplitude was small (not exceeding 0.05°). The root-mean square value of the wing-tip bending deformation at the mid-chord was about $0.05c$, which is equivalent to roughly one vortex core radius.

Figure 18 shows the time-averaged vorticity patterns, probability of instantaneous vortex location, and the frequency spectra of the velocity fluctuations for this close interaction case, in both upstream and downstream crossflow planes, $x/c = -1.05$ and $x/c = 0.05$, for $\alpha_{LW} = 10°$, $\alpha_{TW} = 5°$, $\Delta y/c = 0$, and $\Delta z/c = 0.6$. The distribution of the meandering probability roughly agrees with the shape of the time-averaged vorticity pattern. In the upstream plane, the leading vortex meandering pattern

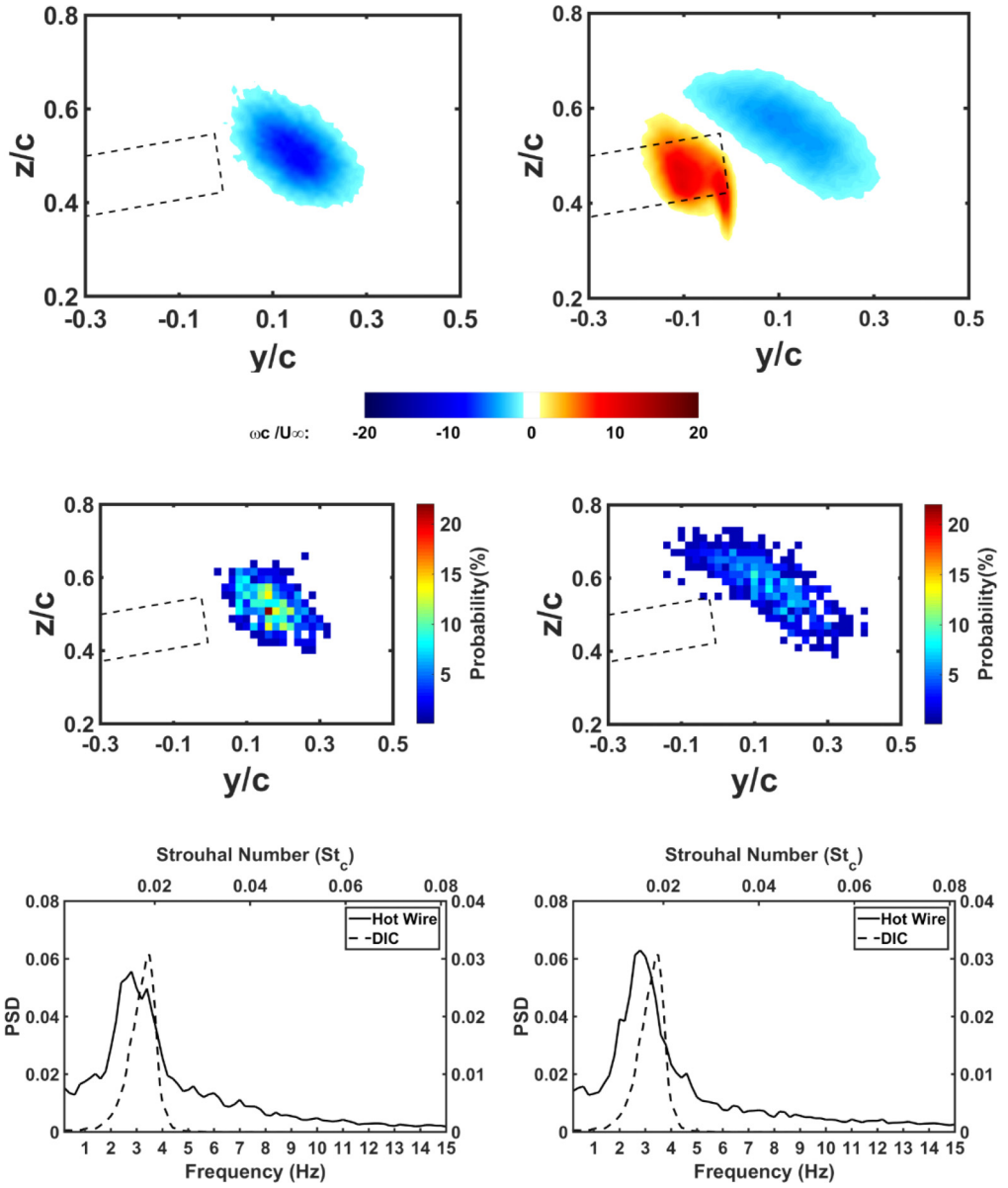

FIG. 18. Time-averaged vorticity patterns (top), probability of instantaneous location of leading vortex (middle), and frequency spectra of the velocity (hot-wire probe location $y/c = 0.2$, $z/c = 0.5$) and wing-tip deflection at midchord in the upstream plane $x/c = -1.05$ (left) and downstream plane $x/c = 0.05$ (right). $\alpha_{\mathrm{LW}} = 10^{\circ}$, $\alpha_{\mathrm{TW}} = 5^{\circ}$, $\Delta y/c = 0$, and $\Delta z/c = 0.6$.

and peak probability resemble those of the rigid interaction cases. However, in the downstream plane the probability distribution is more spread out, without a significant peak. The elongated pattern is slightly wider, without an obvious high probability path. The frequency spectra of the velocity fluctuations in both planes suggest very similar dominant frequency of the vortex meandering as in the rigid case. (The hot-wire probe is located at $y/c = 0.2$, $z/c = 0.5$). Spectra of the wing-tip deflection at midchord (shown with dashed lines) superimposed on these plots reveal that the flexible wing oscillates at a slightly higher frequency, about 3.5 Hz. This implies that the vortex

meandering behavior is not influenced by the oscillations of the flexible wing, but rather is an inherent characteristic of the incident vortex. There is no evidence of coupling between the wing oscillations and vortex meandering in this case. In the numerical simulations of the interaction of flexible wings with streamwise vortices, Barnes *et al.* [30,31] also found that the static (time-averaged) deformation and the resulting repositioning of the incident vortex, rather than the wing oscillations, had a more significant impact on the interaction.

IV. CONCLUSIONS

The interaction of trailing vortices with rigid and flexible downstream wings was investigated experimentally using particle image velocimetry, hot-wire, force, and deformation measurements in a wind tunnel. Counter-rotating upstream vortices may exhibit substantially increased meandering when the upstream vortex is near the wing tip and forms a vortex pair with the trailing vortex shed from the downstream wing. This flow configuration is observed when the leading wing tip is located slightly outboard of the downstream wing tip and produces the largest lift fluctuations. There is also large mean lift increase in this case. In contrast, co-rotating upstream vortices do not exhibit this behavior. The pair of counter-rotating vortices have been found to meander around the wing tip regardless of the ratio of the strengths of the vortices in our experiments. Evidence suggests that meandering of the vortex pair occurs at the natural frequency of the isolated vortex, which corresponds to the first helical mode as suggested by the POD analysis. This is a very long wavelength instability (wavelength to vortex core radius ratio on the order of 10^3), hence with a low Strouhal number based on the wing chord length. Even though some three-dimensionality of the interaction is evident, the dominant frequency remains the same. The effect of meandering is evident in the dominant POD modes just downstream of the wing. The statistical analysis of instantaneous vortex pairs showed that the vortex separation distance is highly correlated with the displacement of the upstream vortex. While the upstream vortex experiences a slight expansion of the core size and some decrease of vorticity in the core, there are highly correlated variations of the core vorticity and circulation of the trailing vortex with the meandering motion of the pair around the wing. The interaction of a flexible wing exhibits similar behavior to that of the rigid wing cases. The wing oscillations have no effect on the meandering frequency, which is determined by the meandering instability that exists upstream. Even for large wing oscillations on the order of one vortex core radius, we have found no evidence of coupling between the wing vibrations and the incident vortex.

ACKNOWLEDGMENTS

The authors acknowledge the EPSRC Grant No. EP/F026099/1 “Equipment for Multiple Projects: Testing and Visualization for Aerospace Research” and the EPSRC strategic equipment Grants No. EP/K040391/1 and No. EP/M000559/1.

[1] D. Hummel, Aerodynamics aspects of formation flight in birds, J. Theor. Biol. **104**, 321 (1983).
[2] S. Lissaman and C. A. Shollenberger, Formation flight of birds, Science, **168**, 1003 (1970).
[3] Z. A. Bangash, R. P. Sanchez, and A. Ahmed, Aerodynamics of formation flight, J. Aircr. **43**, 907 (2006).
[4] J. E. Kless, M. J. Aftosmis, S. A. Ning, and M. Nemec, Inviscid analysis of extended-formation flight, AIAA J. **51**, 1703 (2013).
[5] D. G. Mabey, Similitude relations for buffet and wing rock on delta wings, Prog. Aeronaut. Sci. **33**, 481 (1997).
[6] G. Erickson, J. Schreiner, and L. Rogers, Canard-wing vortex interactions at subsonic through supersonic speeds, in *17th Atmospheric Flight Mechanics Conference, Guidance, Navigation, and Control and Co-located Conferences*, AIAA Paper 1990-2814 (AIAA, Reston, VA, 1990).

[7] D. Rockwell, Vortex-body interactions, Annu. Rev. Fluid Mech. **30**, 199 (1998).
[8] D. J. Garmann and M. R. Visbal, Interactions of a streamwise-oriented vortex with a finite wing, J. Fluid Mech. **767**, 782 (2015).
[9] C. J. Barnes, M. R. Visbal, and R. E. Gordnier, Analysis of streamwise-oriented vortex interactions for two wings in close proximity, Phys. Fluids **27**, 015103 (2015).
[10] C. J. Barnes, M. R. Visbal, and P. G. Huang, On the effects of vertical offset and core structure in streamwise-oriented vortex-wing interactions, J. Fluid Mech. **799**, 128 (2016).
[11] C. McKenna, M. Bross, and D. Rockwell, Structure of a streamwise-oriented vortex incident upon a wing, J. Fluid Mech. **816**, 306 (2017).
[12] C. Chen, Z. Wang, and I. Gursul, Experiments on tip vortices interacting with downstream wings, Exp. Fluids (to be published).
[13] C. Chen, Z. Wang, D. J. Cleaver, and I. Gursul, Interaction of trailing vortices with downstream wings, in *54th AIAA Aerospace Sciences Meeting, San Diego, California*, AIAA Paper 2016-1848 (AIAA, Reston, VA, 2016).
[14] I. Gursul and W. Xie, Buffeting flows over delta wings, AIAA J. **37**, 58 (1999).
[15] I. Gursul and W. Xie, Interaction of vortex breakdown with an oscillating fin, AIAA J. **39**, 438 (2001).
[16] S. Leibovich, Vortex stability and breakdown: Survey and extension, AIAA J. **22**, 1192 (1984).
[17] L. Graftieaux, M. Michard, and N. Grosjean, Combining PIV, POD and vortex identification algorithms for the study of unsteady turbulent swirling flows, Meas. Sci. Technol. **12**, 1422 (2001).
[18] L. Jacquin, D. Fabre, D. Sipp, and E. Coustols, Unsteadiness, instability, and turbulence in trailing vortices, C. R. Physique **6**, 399 (2005).
[19] A. Antkowiak and P. Brancher, Transient energy growth for the Lamb-Oseen vortex, Phys. Fluids **16**, 1 (2004).
[20] A. M. Edstrand, T. B. Davis, P. J. Schmid, K. Taira, and L. N. Cattafesta III, On the mechanism of trailing vortex wandering, J. Fluid Mech. **801**, R1 (2016).
[21] C. Roy and T. Leweke, Experiments on vortex meandering, FAR-Wake Technical Report AST4-CT-2005-012238, CNRS-IRPHE (2005); also presented in International Workshop on Fundamental Issues related to Aircraft Trailing Wakes (2008).
[22] C. del Pino, J. M. Lopez-Alonso, L. Parras, and R. Fernandez-Feria, Dynamics of the wing-tip vortex in the near field of a NACA 0012 aerofoil, Aeronaut. J. **115**, 229 (2011).
[23] X. Zhang, Z. Wang, and I. Gursul, Interaction of multiple vortices over a double delta wing, Aerosp. Sci. Technol. **48**, 291 (2016).
[24] B. F. Ma, Z. Wang, and I. Gursul, Symmetry breaking and instabilities of conical vortex pairs over slender delta wings, J. Fluid Mech. **832**, 41 (2017).
[25] L. Sirovich, Turbulence and the dynamics of coherent structures. I. Coherent structures, Q. Appl. Math. **45**, 561 (1987).
[26] H. Chen, D. L. Reuss, L. S. Hung, and S. Sick, A practical guide for using proper orthogonal decomposition in engine research, Int. J. Engine Res. **14**, 307 (2012).
[27] Z. Wang and I. Gursul, Unsteady characteristics of inlet vortices, Exp. Fluids **53**, 1015 (2012).
[28] D. S. Pradeep and F. Hussain, Transient growth of perturbations in a vortex column, J. Fluid Mech. **550**, 251 (2006).
[29] C. J. Heaton and N. Peake, Transient growth in vortices with axial flow, J. Fluid Mech. **587**, 271 (2007).
[30] C. J. Barnes, M. R. Visbal, and R. E. Gordnier, Investigation of aeroelastic effects in streamwise-oriented vortex/wing interactions, in *52nd Aerospace Sciences Meeting, 13–17 January 2014, Maryland*, AIAA Paper 2014-1281 (AIAA, Reston, VA, 2014).
[31] C. J. Barnes, M. R. Visbal, and G. P. Huang, Numerical simulations of streamwise-oriented vortex/flexible wing interactions, in *44th AIAA Fluid Dynamics Conference, 16–20 June 2014, Atlanta*, AIAA Paper 2014-2313 (AIAA, Reston, VA, 2014).